Supplementary Information: "First-principles investigation of sulfur and sulfur-oxide compounds as potential optically active defects on (6,5) SWCNT"

Tina N Mihm,[†] Kasidet Jing Trerayapiwat,[‡] Xinxin Li,[¶] Xuedan Ma,[¶] and Sahar Sharifzadeh[*,†]

†*Department of Electrical and Computer Engineering, Boston University, MA, 02215, USA*

‡*Department of Chemistry, Boston University, MA, 02215, USA*

¶*Center for Nanoscale Materials, Argonne National Laboratory, Lemont, IL 60439, USA*

§*Consortium for Advanced Science and Engineering, University of Chicago, Chicago, IL 60637, USA*

‖*Materials Science and NanoEngineering, Rice University, Houston, TX, 77251, USA*

⊥*Northwestern Argonne Institute of Science and Engineering, Evanston, IL 60208, USA*

#*Department of Chemistry, Boston University, Boston, MA, 02215, USA*

@*Materials Science Division, Boston University, Boston, MA, 02215, USA*

△*Department of Physics, Boston University, Boston, MA, 02215, USA*

E-mail: ssharifz@bu.edu

1 Experimental photoluminescence spectrum of SOx-defective (6,5) SWCNT

1.1 Experimental Details

Chirality-sorted (6,5) single walled carbon nanotubes (SWCNTs) were prepared using a two-step phase separation method, as previously described,[1,2], and transferred into a 1 wt% sodium dodecyl sulfate (SDS) solution via pressure filtration. The samples were subsequently diluted to an optical density of approximately 0.1 at the E_{11} absorption peak of the (6,5) SWCNTs by 0.5 wt% SDS solutions. Functionalization of the SWCNTs was carried out using a mixture of sodium bicarbonate and sodium dithionite. The functionalized solution was then stored in the dark for further optical characterizations.

Absorption spectra were measured using a Varian Cary 50 UV-Vis spectrophotometer. Photoluminescence spectra were obtained with a Nanolog spectrofluorometer (Horiba Jobin Yvon), which is equipped with a liquid nitrogen-cooled InGaAs detector.

1.2 Photoluminescence Spectrum

Figure S.1 presents the raw photoluminescence (PL) data while Figure S.2 presents a comparison of the SO_x -doped and undoped (pristine) (6,5) SWCNT. For both systems, there is a peak at $\sim$ 984 nm (1.26 eV), which is consistent with the pristine tube lowest energy E_{11} peak.[3] With the introduction of the defect, this peak is reduced in intensity compared with a high energy at at 1105 nm (1.12 eV) with a low-energy shoulder at 1228 nm (1.0 eV). These new transitions introduced at $0.1 - 0.3$ eV below the pristine gap are consistent with the E_{11}^* transition previously reported for other sp^2 and sp^3 doped (6,5) SWCNT.[4–9] We note that there is a low-intensity peak at $\sim$ 1130 nm in the pristine tube spectrum; this peak is attributed to unintentional doping that is known to occur in the SWCNT due to exposure to oxygen in the air during preparation[10,11]. The details of synthesis and characterization of

this system will be published elsewhere.

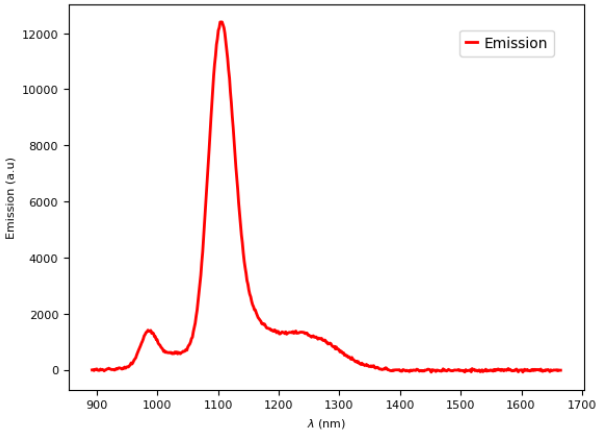

Figure S.1: Photoluminescence spectrum of (6,5) SWCNT after exposure to sodium dithionite.

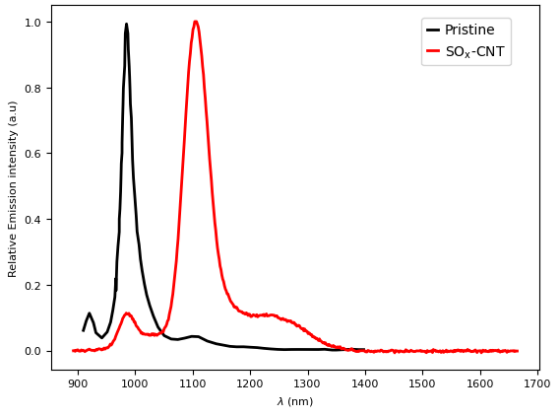

Figure S.2: Photoluminescence spectrum of pristine (6,5) SWCNT and (6,5) SWCNT after exposure to sodium dithionite. The data for each plot was normalized such that the maximum intensity is 1 (see Supplementary Materials Fig S.1 for measured spectrum of the doped SWCNT). The pristine spectrum was extracted from Ref 5.

2 Binding information for SO_x adsorbates

2.1 Unbound structures

In addition to the binding described in the main text, we tested structures for SO, SO_2 and SO_3 that were found to be unbound and therefore not presented in the manuscript. For the SO molecule, epoxide-type binding was considered in addition to structure 3 of Figure

2(a) of the main text. In addition to the weakly bound SO_2, Line-H sidewall system shown in the main text, we also studied the binding of this system on a tube containing a single carbon vacancy, but found the presence of the vacancy resulted in an unbound SO_2. For SO_3 , in addition to the flat-type binding shown in Figure 2(a) of the main text, we tested an OO-loop-type binding and ether-type binding where the SO_3 binds onto the $1, 3$ carbons in the hollow site.

2.2 Binding configuration of sulfur in the thioether-l position

We considered two binding positions for the thioether-l positions for the sulfur adsorbate to test how the chiral nature of the tube affects the binding as shown in Fig. S.3. Position 1 had the sulfur placed along the top, right carbons, offset from the chirallity of the tube, while Position 2 has the sulfur placed between the bottom right carbons, putting it in line with the chirality of the nanotube.

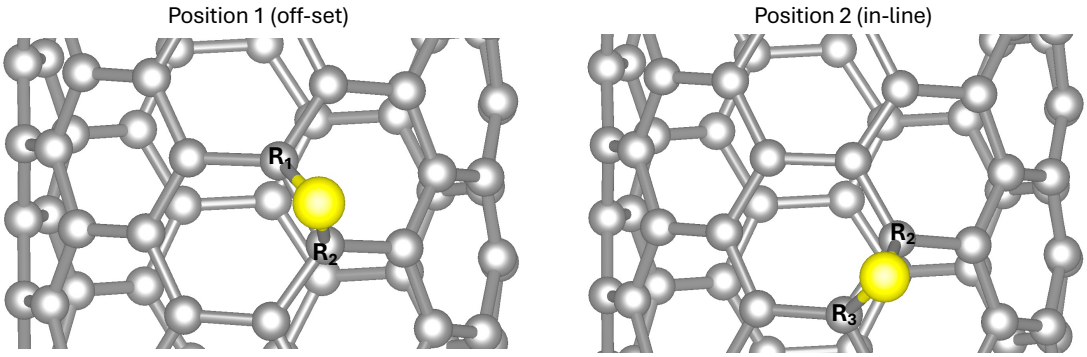

Figure S.3: Final bound structures for the two S, thioether-l positions considered in the main text. Both structures optimize to the Episulfide-l structure.

2.3 Detailed binding information for adsorbates studied

Table S.1 presents detailed bonding information for all adsorbates studied, including bond angles, bond lengths and distance from the SWCNT surface.

Table S.1: Bond lengths [Å], distance from the SWCNT surface (h_s) [Å], and bond angles [o] for all adsorbates considered.

System	R_1 - X	R_2 - X	R_1 - R_2	h_s	S-R_1-R_2	R_1-S-R_2	S-R_2-R_1	O_1-S-O_2
S, Episulfide-l, off-set	1.88	1.88	1.50	–	66.42	47.15	66.43	–
S, Episulfide-l, in-line	1.88	1.88	1.51	–	66.33	47.33	66.33	–
S, Episulfide-d	1.83	1.83	1.63	–	63.55	52.89	63.55	–
S, Thioether-d	1.76	1.76	2.26	–	50.21	79.59	50.21	–
SO, 1,2-oxathietane-l	2.08	2.02	1.49	1.91	66.44	42.73	70.83	–
SO,1,2-oxathietane-d	2.10	2.01	1.49	1.91	65.49	42.55	71.96	–
SO2, OO-loop-d	3.19	3.32	1.43	3.16	82.45	25.27	72.30	118.73
SO2, Episulfide-d	3.19	3.22	1.43	3.13	78.34	25.71	75.95	118.70
SO2, Line-H	2.93	3.33	1.41	2.92	61.17	25.01	93.82	117.46
SO3, flat	–	–	–	3.03	–	–	93.98	119.91
CNT-H, Line-H	–	1.12	–	–	–	–	–	–

2.4 Charge transfer between molecule and adsorbate

Figure S.4 presents the calculated charge density differences for the five defect systems shown in Figure 4 in the main text. For S and SO, there is indication of charge sharing between the adsorbate and SWCNT, as expected for chemical bonding. For both SO_2 and SO_3 , there is no indication of charge sharing. For SO_2 , there is charge redistribution within the tube while for SO_3 , the charge redistribution is within the molecule only.

3 Bandstructure and projected density of states for all bound S and SO_x adsorbates

Figure S.7 presents the defective SWCNT bandstructure for the ten bound absorbates presented in the main text. Figures S.7 b, d, f, h, and j are presented in Figure 4 of the main text. Figure S.5 presents the projected density of states (PDOS) for all ten adsorbates studied in this work. The PDOS confirms that for S and SO, there is charge sharing between adsorbate and SWCNT with sulfur and oxygen orbital mixing with carbon orbitals (Figure S.5a-e). For unpassivated SO_2 (Figure S.5 f-g), S and O p-orbital density is only present within the defect band, right below the conduction band. For passivated SO_2 (Figure S.5h), there is a single peak at the VBM associated with the bound hydrogen and the S/O p-orbitals overlap

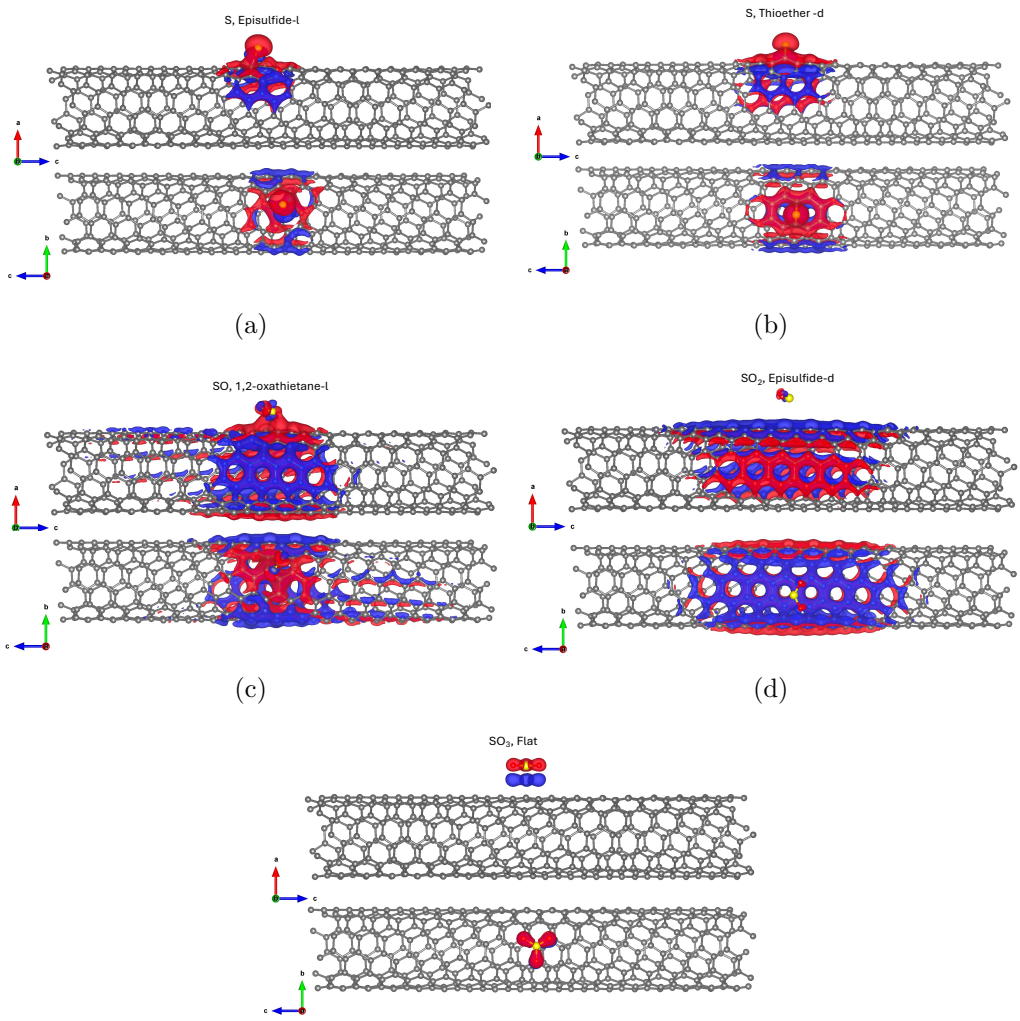

Figure S.4: Electronic charge density differences for the (a) S, episulfide-l, (b) S, thioether-d, (c) SO , (d) SO_2 and (e) SO_3 ligands. Each system has been labeled with the ligand orientation, which also corresponds to the band structures in Fig 4 in the main text. The isosurface is chosen such that it captures 40% of the density. The charge differences are colored to show positive electronic difference (red) and negative electronic difference (blue) based on electron density. The charge density differences are shown from two different perspectives: on-top (top) and from the side of the tube (bottom).

slightly with the SWCNT conduction band. The SO_3 system shown in (i) also shows overlap between the S/O p-orbital densities with the CNT conduction band, which we attribute to possible artificial mixing of the bands due to the delocalization of error of DFT.

Figure S.6 presents the band splitting in the valence (Fig. 6(a)) and conduction (Fig. 6(b))bands for the pristine and five doped systems shown in Figure 4 in the main text along the Brillouin Zone path. Both plots show that there is significant band splitting in the presence of the S

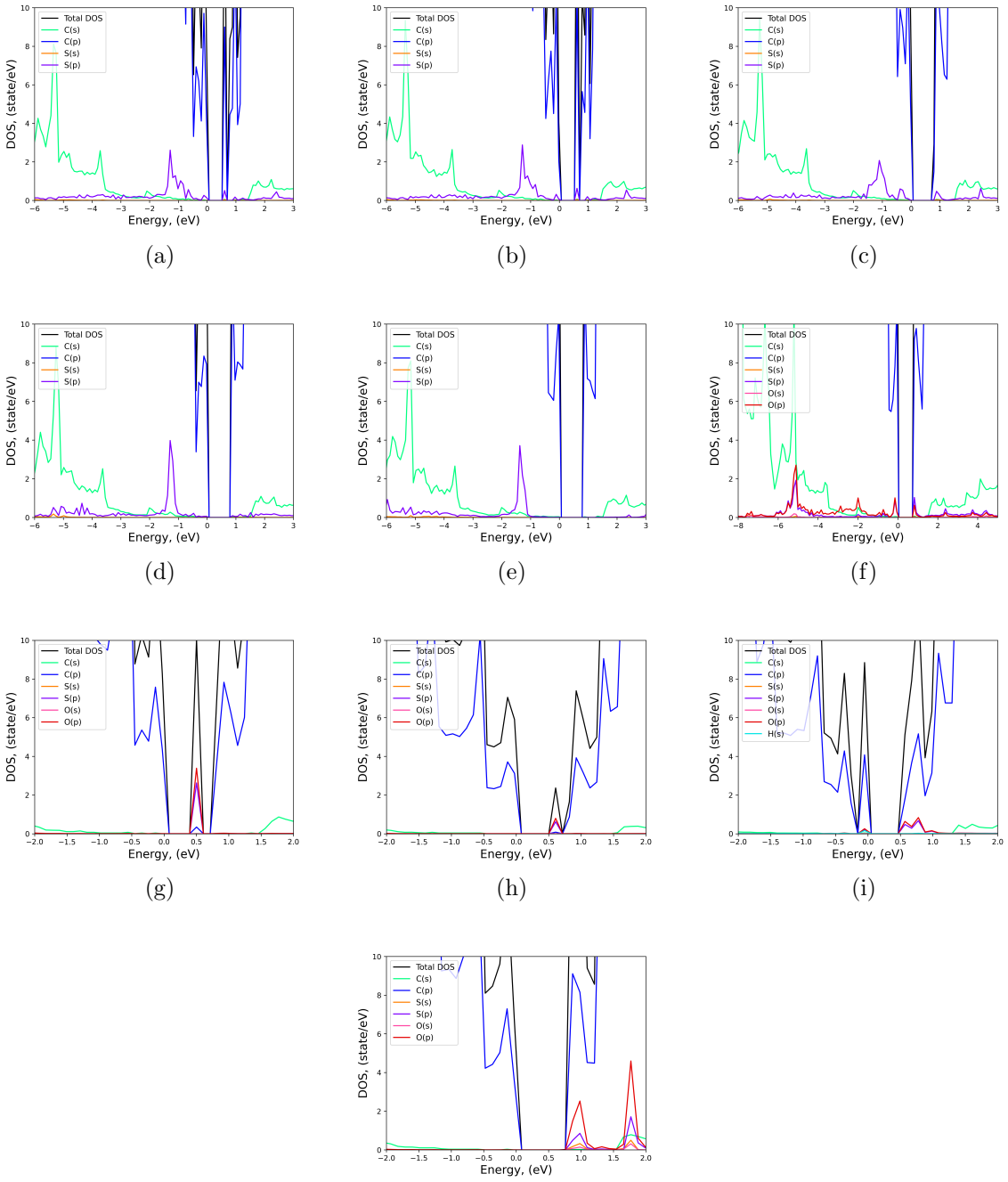

Figure S.5: Projected density of states (PDOS) for (a) S, episulfide-l, (b) S, thioether-l, offset, (c) S, thioether-l, in-line, (d) S, episulfide-d, (e) S, thioether-d ,(f) SO, 1,2-oxathietane-l, (g) SO_2 , OO-loop-d, (h) SO_2 , episulfide-l, (i) SO_2 , line-H, and (j) SO_3 , flat. All graphs have been zeroed to the valence band maximum (VBM).

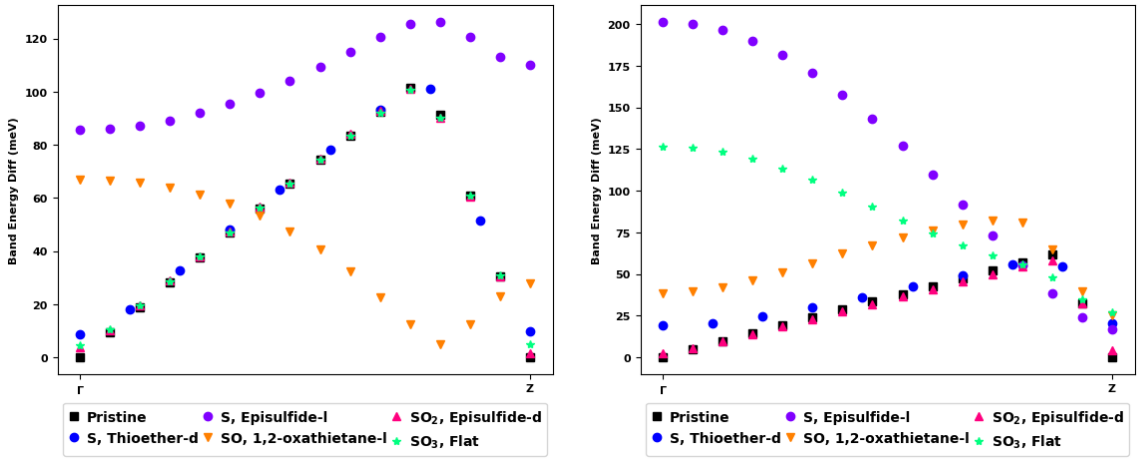

(a) (b)

Figure S.6: Band energy difference between the (a) valence band max (VBM) and VBM-1 bands and the (b) conduction band min (CBM) and CBM+1 bands of the SWCNT for the pristine system compared to the five different adsorbates shown in Figure 4 in the main text. All energy differences are shown as absolute values.

and SO adsorbates in the valence and conduction bands, while the SO_2 adsorbate show very little band splitting and SO_3 only shows splitting in the conduction band.

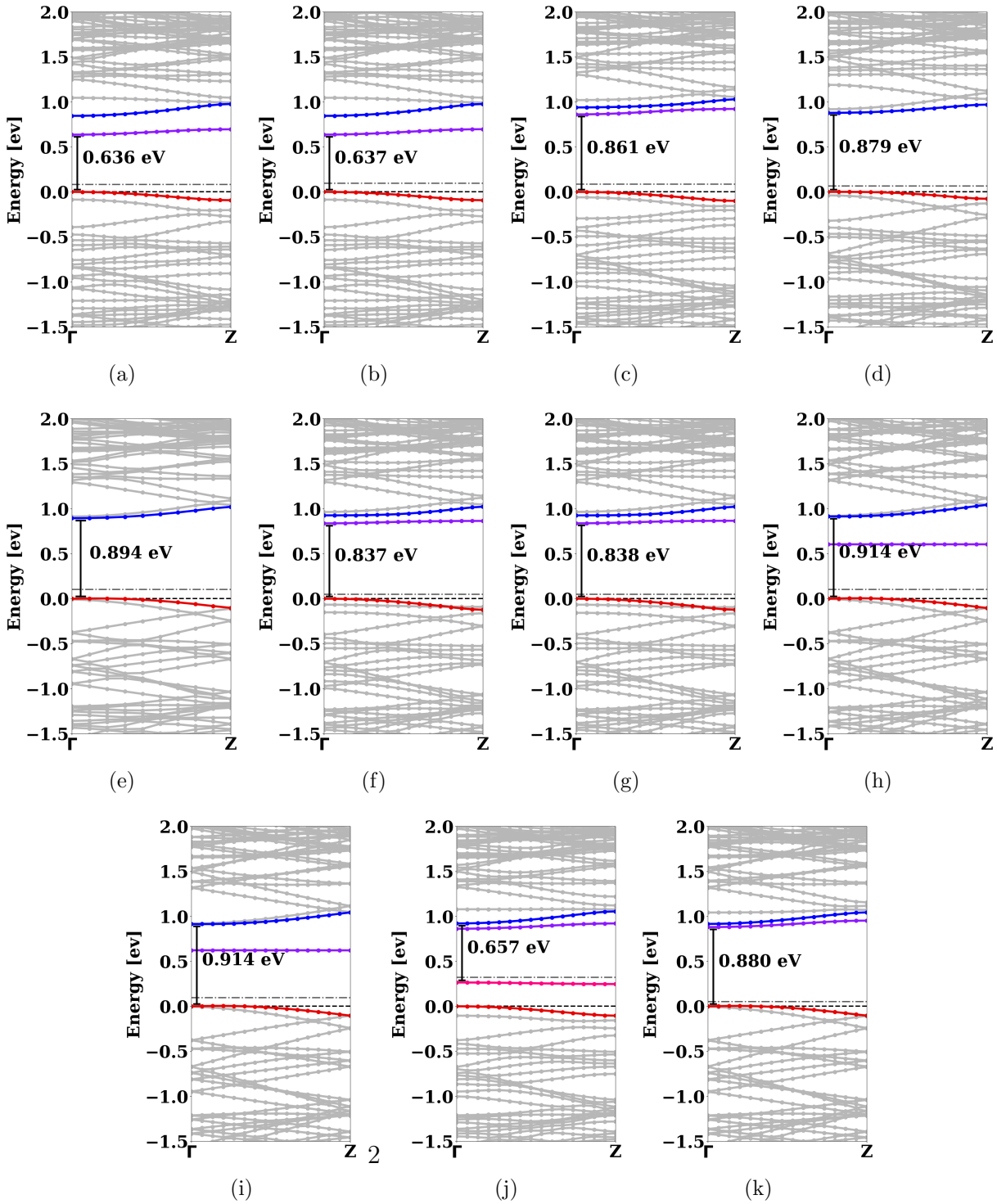

Figure S.7: Band structures for (a) S, episulfide-l, (b) S, thioether-l, off-set, (c) S, thioether-l, in-line, (d) S, episulfide-d, (e) S, thioether-d ,(f) SO, 1,2-oxathietane-d, (g) SO, 1,2-oxathietane-l, (h) SO_2 , OO-loop-d, (i) SO_2 , episulfide-l, (j) SO_2 , line-H, and (k) SO_3 , flat. Occupied pristine-like valence bands and unoccupied conduction bands are shown in red and blue, respectively, while unoccupied states localized on the defect are in purple. The gray dash-dot line on each band structure represents the Fermi energy level. All plots are shifted such that the top of the pristine-like valence band is at zero at $\mathbf{k} = 0$ (indicated by black dash line).

4 Comparison of SO_x with previously reported covalent defects

Table S.2 shows a comparison of the properties of different sp3 defects on a(6,5)-SWCNT obtained using DFT. The table shows the binding energies (E_b) and the difference between the pristine SWCNT band gap and the defect SWCNT band gap ($\Delta E_{gap} = E_{pristine} - E_{defect}$) in eV for each kind of defect. The DFT functional that was used in the study is also specified to allow for proper comparison across studies.

Table S.2: DFT-predicted properties of covalent defects from this work compared to previous studies. The binding energy (E_b) and difference between the pristine and defect band gap (ΔE_{gap}) are given in eV along with the DFT functional used for each study.

Sp3-dopant	E_b	ΔE_{gap}	DFT functional	Referance
S, Episulfide-l, off-set	-1.53	0.28	PBE	This work
S, Episulfide-l, in-line	-1.57	0.05	PBE	This work
S, Episulfide-d	-1.69	0.04	PBE	This work
S, Thioether-d	-1.82	0.01	PBE	This work
SO	-0.56	0.08	PBE	This work
SO_2	-0.2	0.00	PBE	This work
SO_2, Line-H	-0.33	0.26	PBE	This work
SO_3	-0.27	0.00	PBE	This work
O, epoxide-l	-3.75	0.25	AM1 Hamiltonian [a], TDDFT/B3LYP [b]	Ref 4
O, ether-l	-2.81	-0.01	AM1 Hamiltonian [a], TDDFT/B3LYP [b]	Ref 4
O, ether-d	-5.28	0.06	AM1 Hamiltonian [a], TDDFT/B3LYP [b]	Ref 4
aryl functional groups, unpassivated	–	0.27 - 0.30	LDA	Ref 12
Pd-containing functional groups	–	0.31 - 0.65	LDA	Ref 12
H, *ortho*	–	$\sim$ 0.05 - 0.09	AM1 Hamiltonian [a], TDDFT/B3LYP [b]	Ref 13
H, *para*	–	$\sim$ 0.03 - 0.17	AM1 Hamiltonian [a], TDDFT/B3LYP [b]	Ref 13
two methyl *ortho* defects groups	–	0.15 - 0.25	CAM-B3LYP	Ref 14
aryl and alkyl functional groups (with EW groups), passivated	–	0.13 - 0.20	CAM-B3LYP	Ref 15
diaryl and aryl-H functional groups, *ortho* , passivated	–	0.04 - 0.30	CAM-B3LYP	Ref 16
diaryl and aryl-H functional groups, *para*, passivated	–	0.0 - 0.35	CAM-B3LYP	Ref 16
aryl diazonium cation (physisorb), with and without solvent	-0.55 to -1.61	0.1–1.36	B3LYP / wB97XD	Ref 17
aryl diazonium radical, with and without solvent	–	0.13 - 0.18	B3LYP / wB97XD	Ref 17
Double aryl diazonium radical, with and without solvent	–	-0.05	B3LYP / wB97XD	Ref 17

[a] Used for E_b and structure optimization, [b] Used for E_{gap}

As demonstrated in Table S.2, the binding of sulfur defects show similar trends to the oxygen defects. For both the oxygen and sulfur defects, the ether-d binding orientation binds the strongest; additionally, the "l" orientation binding strengths show the same variation based on location and the type of bond between the dopant and the tube. The trend in the bandgaps associated with each orientation is also similar, consistent with the similar photoluminescence energies measured for both defects.[18]

5 PBE vs HSE06 DFT functionals

Table S.3: The binding energy and band gaps for HSE06 compared to PBE for three SO_x defects

	HSE06				PBE		
Structure	E_{gap} (eV)	ΔE_{gap} (meV)	E_b (eV)	ΔE_b (eV)	ΔE_{gap} (meV)	E_b (eV)	ΔE_b (eV)
Pristine	1.155	0	–	0	–	–	–
1,2-oxathietane-d	1.092	63.5	-0.19	2.38	80	-0.56	1.26
Thioether-d	1.130	27.20	-2.57	0.0	283	-1.82	0.0
Episulfide-l, off-set	0.852	303	-2.29	0.28	26	-1.53	0.29

Table S.3 shows the results of the hybrid HSE06 calculations to compare to our PBE results for the binding energy and band gaps for three of our defects. As with the PBE calculations, we ran the hybrid HSE06 calculations using the Vienna Ab initio Simulation Package (VASP) and frozen core potentials as described within the projector-augmented wave method (PAW). Due to computational cost, we used the optimized structures from PBE and calculated the adsorption energy within HSE06. Binding energies were calculated in the same way as the PBE calculations (see methods section in the main text). All energies were converged to below 1×10^{-6} eV. The ΔE_b shows the relative difference in the binding energies with respect to the lowest binding energy structure, thioether-d. Both HSE06 and PBE show the same trend in binding energies, with thioether-d being the strongest bound and 1,2-oxathietane-d being the weakest bound. We note that PBE may slightly over-bind 1,2-oxathietane-d.

The table also shows the band gaps for HSE06 vs PBE for the three defects and the pristine tube. HSE06 and PBE both show similar shift in the bands. Both these results and the binding energies in the previous table demonstrate that, given that HSE06 is quite a bit more expensive to run, PBE provides an acceptable approximation for understanding trends.

Table S.4: Band gap comparison for different methods considered: DFT-PBE, HSE06, MBPT within the GW approximation, which predicts the fundamental gap, and GW/BSE which predicts the optical gap.

System	PBE (eV)	HSE06 (eV)	GW (eV)	GW/BSE (eV)	Δ PBE (meV)	Δ HSE06 (meV)	Δ GW (meV)	Δ GW/BSE (meV)
episulfide-d	0.894	1.128	2.023	1.005	20	27	52	39
pristine	0.914	1.155	2.075	1.044	0	0	0	0

Table S.4 shows the results of MBPT within the GW/BSE approximation for the thioether-d configuration and pristine system compared to two DFT functionals. All three methods indicate a slight red-shift of the gap upon adsorption of the thioether-d. While many-body effects increase this shift, exciton binding reduces the shift slightly, with GW/BSE agreeing well with HSE06. The conclusion of our study is unchanged regardless of the level of theory.

6 PBE k-point convergence testing

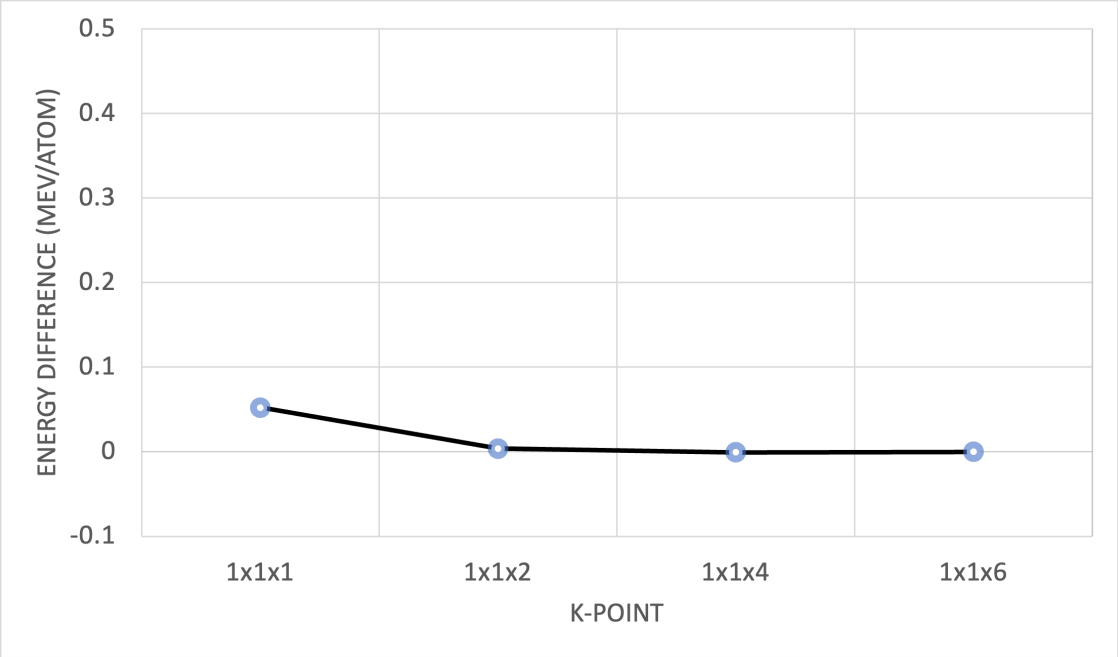

Figure S.8: K-point convergence data for increasing k-point shown as the difference in meV/atom to the largest k-point grid.

Fig. S.8 shows the data for the convergence of the total energy with respect to the k-point mesh for the pristine SWCNT. The energy differences shown in the figure were taken with respect to the largest k-point mesh ($1 \times 1 \times 6$) and show that the energy for the pristine tube is converged to less than 1 meV for all k-point meshes tested.

References

(1) Chen, J.-S.; Trerayapiwat, K. J.; Sun, L.; Krzyaniak, M. D.; Wasielewski, M. R.; Rajh, T.; Sharifzadeh, S.; Ma, X. Long-lived electronic spin qubits in single-walled carbon nanotubes. *Nature Communications* **2023**, *14*, 848.

(2) Chen, J.-S.; Dasgupta, A.; Morrow, D. J.; Emmanuele, R.; Marks, T. J.; Hersam, M. C.; Ma, X. Room Temperature Lasing from Semiconducting Single-Walled Carbon Nanotubes. *ACS Nano* **2022**, *16*, 16776–16783.

(3) Bachilo, S. M.; Strano, M. S.; Kittrell, C.; Hauge, R. H.; Smalley, R. E.; Weisman, R. B. Structure-Assigned Optical Spectra of Single-Walled Carbon Nanotubes. *Science* **2002**, *298*, 2361–2366, Publisher: American Association for the Advancement of Science.

(4) Ma, X.; Adamska, L.; Yamaguchi, H.; Yalcin, S. E.; Tretiak, S.; Doorn, S. K.; Htoon, H. Electronic Structure and Chemical Nature of Oxygen Dopant States in Carbon Nanotubes. *ACS Nano* **2014**, *8*, 10782–10789.

(5) Ghosh, S.; Bachilo, S. M.; Simonette, R. A.; Beckingham, K. M.; Weisman, R. B. Oxygen Doping Modifies Near-Infrared Band Gaps in Fluorescent Single-Walled Carbon Nanotubes. *Science* **2010**, *330*, 1656–1659.

(6) Hartmann, N. F.; Yalcin, S. E.; Adamska, L.; Hároz, E. H.; Ma, X.; Tretiak, S.; Htoon, H.; Doorn, S. K. Photoluminescence imaging of solitary dopant sites in covalently doped single-wall carbon nanotubes. *Nanoscale* **2015**, *7*, 20521–20530.

(7) Trerayapiwat, K. J.; Li, X.; Ma, X.; Sharifzadeh, S. Broken Symmetry Optical Transitions in (6,5) Single-Walled Carbon Nanotubes Containing sp3 Defects Revealed by First-Principles Theory. *Nano Letters* **2024**, *24*, 667–671.

(8) Setaro, A.; Adeli, M.; Glaeske, M.; Przyrembel, D.; Bisswanger, T.; Gordeev, G.; Maschietto, F.; Faghani, A.; Paulus, B.; Weinelt, M.; Arenal, R.; Haag, R.; Reich, S.

Preserving -conjugation in covalently functionalized carbon nanotubes for optoelectronic applications. *Nature Communications* **2017**, *8*, 14281, Publisher: Nature Publishing Group.

(9) Hayashi, K.; Niidome, Y.; Shiga, T.; Yu, B.; Nakagawa, Y.; Janas, D.; Fujigaya, T.; Shiraki, T. Azide modification forming luminescent sp^2 defects on single-walled carbon nanotubes for near-infrared defect photoluminescence. *Chemical Communications* **2022**, *58*, 11422–11425.

(10) McClain, D.; Thomas, N.; Youkey, S.; Schaller, R.; Jiao, J.; O'Brien, K. P. Impact of oxygen adsorption on a population of mass produced carbon nanotube field effect transistors. *Carbon* **2009**, *47*, 1493–1500.

(11) Collins, P. G.; Bradley, K.; Ishigami, M.; Zettl, A. Extreme Oxygen Sensitivity of Electronic Properties of Carbon Nanotubes. *Science* **2000**, *287*, 1801–1804, Publisher: American Association for the Advancement of Science.

(12) Trerayapiwat, K. J.; Lohmann, S.; Ma, X.; Sharifzadeh, S. Tuning spin–orbit coupling in (6,5) single-walled carbon nanotube doped with sp3 defects. *Journal of Applied Physics* **2021**, *129*, 014309.

(13) Kilina, S.; Ramirez, J.; Tretiak, S. Brightening of the Lowest Exciton in Carbon Nanotubes via Chemical Functionalization. *Nano Letters* **2012**, *12*, 2306–2312.

(14) Weight, B. M.; Sifain, A. E.; Gifford, B. J.; Kilin, D.; Kilina, S.; Tretiak, S. Coupling between Emissive Defects on Carbon Nanotubes: Modeling Insights. *The Journal of Physical Chemistry Letters* **2021**, *12*, 7846–7853.

(15) Gifford, B. J.; He, X.; Kim, M.; Kwon, H.; Saha, A.; Sifain, A. E.; Wang, Y.; Htoon, H.; Kilina, S.; Doorn, S. K.; Tretiak, S. Optical Effects of Divalent Functionalization of Carbon Nanotubes. *Chemistry of Materials* **2019**, *31*, 6950–6961, Publisher: American Chemical Society.

(16) Gifford, B. J.; Kilina, S.; Htoon, H.; Doorn, S. K.; Tretiak, S. Exciton Localization and Optical Emission in Aryl-Functionalized Carbon Nanotubes. *The Journal of Physical Chemistry C* **2018**, *122*, 1828–1838, Publisher: American Chemical Society.

(17) Ramirez, J.; Mayo, M. L.; Kilina, S.; Tretiak, S. Electronic structure and optical spectra of semiconducting carbon nanotubes functionalized by diazonium salts. *Chemical Physics* **2013**, *413*, 89–101.

(18) Li, X.; Mihm, T. N.; Chen, J.-S.; Hou, H.; Wen, J.; Sharifzadeh, S.; Ma, X. Near-Infrared Emission from Sulfur Heteroatom Defects in Single-Walled Carbon Nanotubes. *The Journal of Physical Chemistry C* **2025**, *129*, 17590–17598, Publisher: American Chemical Society.